Materials Characterization 142 (2018) 237–244

Contents lists available at ScienceDirect

Materials Characterization

journal homepage: www.elsevier.com/locate/matchar

Structure, magnetic and cytotoxic behaviour of solvothermally grown Fe_3O_4@Au core-shell nanoparticles

A. Ángeles-Pascual[a,*], J.R. Piñón-Hernández[b], M. Estevez-González[b], U. Pal[c], S. Velumani[d], R. Pérez[b], R. Esparza[b,*]

[a] Laboratorio Avanzado de Nanoscopía Electrónica (LANE), Centro de Investigación y de Estudios Avanzados del I.P.N., Av. Instituto Politécnico Nacional 2508 Col. San Pedro Zacatenco, México D.F. 07360, Mexico
[b] Centro de Física Aplicada y Tecnología Avanzada, Universidad Nacional Autónoma de México, Boulevard Juriquilla 3001, Santiago de Querétaro, Qro. 76230, Mexico
[c] Instituto de Física, Benemérita Universidad Autónoma de Puebla, Apdo. Postal J-48, Puebla, Pue. 72570, Mexico
[d] Departamento de Ingeniería Eléctrica, Centro de Investigación y de Estudios Avanzados del I.P.N., Av. Instituto Politécnico Nacional 2508 Col. San Pedro Zacatenco, México D.F. 07360, Mexico

ARTICLE INFO

Keywords:
Magnetic nanoparticles
Core-shell
Electron microscopy
Apoptosis assay

ABSTRACT

Magnetic nanoparticles (MNPs) have demonstrated their potential in a wide variety of biomedical applications including in tumour hyperthermia. However, highly reactive nature and aggregation affinity of these nanostructures are the principal limitations for such applications. To overcome these limitations, those MNPs should be covered with an inert shell in order to protect the magnetic core against chemical alterations. Considering the noble, chemically inert nature of gold, which also has good biocompatibility, we fabricated chemically stable gold-coated Fe_3O_4 (Fe_3O_4@Au) nanoparticles of 20–50 nm size range with considerable saturation magnetization, though a simple one-pot solvothermal method. The morphology, elemental distribution and the structure of the core-shell nanoparticles were characterized using aberration-corrected (Cs) Scanning transmission electron microscopy (STEM), and compared with their simulated images. Cytotoxicity assay in MDCK cell line was performed to evaluate the biocompatibility of the nanoparticles. The results showed higher cell viability for the Fe_3O_4@Au nanoparticles, suggesting their good biocompatibility and potentials for biomedical applications.

1. Introduction

Magnetic nanoparticles (MNPs) have generated a new trend in the field of advanced materials, mainly due to their multiple biomedical applications [1–3]. Due to their excellent properties, such as superparamagnetic behaviour, good magnetic response, non-toxicity, and biocompatibility [4–6], they have a wide applicability in biomedical fields. Among the MNPs, currently magnetite (Fe_3O_4) nanoparticles have received special attention, mainly as effective heating agents for magnetic hyperthermia therapy [7]. Fe_3O_4 has an inverse spinel structure with alternating octahedral and tetrahedral-octahedral layers, where the Fe^{2+} cations occupy half of the octahedral sites and Fe^{3+} cations occupy tetrahedral sites and half octahedral sites [8]. One important advantage of magnetite NPs is their superparamagnetic nature at room temperature, when their particle size reduces to 20 nm or below [9], with blocking temperature (T_B) increasing with temperature. However, MNPs have tendencies to aggregate and oxidize, reducing their application potentials. For example, magnetite (Fe_3O_4) transforms easily to maghemite (γ-Fe_2O_3) by air annealing at 300 °C [10]. Although both of them have similar crystallographic structure, the saturation magnetization of maghemite is substantially lower than magnetite. Therefore, a detailed structural analysis is necessary, identifying the position and coordination of the atoms in the fabricated MNPs, to evaluate their application potentials. Moreover, the contribution of different electrostatic dispersion agents of organic, inorganic and polymeric (coatings) nature, utilized for the stabilization of MNPs under physiological conditions to enhance their biocompatibility [2,11] should be considered in their structural analysis.

On the other hand, gold nanoparticles (Au NPs), with large specific surface area (surface to volume ratio) have higher number of surface atoms; and hence, higher activities in multiple chemical reactions and catalytic processes. On the other hand, due to plasmonic nature, Au NPs and Au nanoshells exhibit intense surface plasmon resonance (SPR) absorption bands at different energy positions depending their size and shapes, which are attractive for use in cancer therapy [12]. Advantages of utilizing Au NPs for cellular imaging over other materials or compounds have also been reported by several researchers [13–15]. However, for plasmonic photo-thermal therapy (PTT), biomedical imaging

* Corresponding authors.
E-mail addresses: aangelesp@cinvestav.mx (A. Ángeles-Pascual), resparza@fata.unam.mx (R. Esparza).

https://doi.org/10.1016/j.matchar.2018.05.041
Received 25 January 2018; Received in revised form 24 May 2018; Accepted 26 May 2018
Available online 28 May 2018
1044-5803/

or other biomedical applications, evaluation of chemical stability, biocompatibility and bioconjugation of Au NPs (functionalized or not) in physiological environments is essential [16].

Due to adequate magnetic properties of magnetite, and plasmonic nature of gold, which is also a noble metal, Au coated Fe_3O_4 (Au@Fe_3O_4) NPs provide the synergetic effects of both. This hybrid system has several potential applications including neurotransmitter detection [17], photo-thermal elimination of cancer cells, and multimodal cancer imaging [18]. Coating with Au layer not only induces added functionalities to the magnetite nanoparticles, also protects them from undesired oxidation, along with enhancing their chemical and thermal stabilities [19]. Sun et al. have reported a higher catalytic reduction of H_2O_2 by Au@Fe_3O_4 NPs than Au or Fe_3O_4 NPs individually. They found that the improved activity of Fe_3O_4@Au NPs is due to a charge transfer at the Au - Fe_3O_4 interface [20].

Research focus of several research groups has been on the search of effective methods to synthesize stable and homogeneous Fe_3O_4@Au nanoparticles, which have received attention due to their potential applications mainly in the biomedical field [6,21–23]. Gold coating over magnetite nanoparticles provide a suitable platform for adequate functionalization by therapeutic molecules, which is one of the principal challenges for utilizing magnetic Fe_3O_4@Au nanoparticles in cancer therapy [24]. This is because the cancer cells lack of an appropriate heat shock response, therefore die before the normal cells, when the tissue temperature is above 42 °C, and the time required to reach therapeutic temperature is faster for Fe_3O_4@Au compared to bare Fe_3O_4 nanoparticles [25].

Although a considerable amount of work has been reported in the literature on the synthesis of iron oxide nanoparticles and gold coating over them [19,26], only a few of them analyzed their biocompatibility, which is another parameter, necessary to be evaluated before utilizing these hybrid nanostructures for biomedical applications [27,28].

In this paper, we present a detailed structural, magnetic, and cytotoxic evaluation of Fe_3O_4@Au nanoparticles fabricated by a novel, economical and efficient one-pot solvothermal technique. X-ray diffraction (XRD) and scanning transmission electron microscopy (STEM) techniques were used for the structural characterization of the nanostructures. High-angle annular dark-field (HAADF) imaging in STEM, which is a very versatile and useful technique to identify the structure and atomic positions in the compound, has been utilized along with simulated HAADF-STEM images to define the atomic positions, and structural models. The elemental composition of the samples has been analyzed using the STEM-energy-dispersive X-ray spectroscopy (STEM-EDS). Magnetic behaviours of the fabricated Fe_3O_4 and Fe_3O_4@Au NPs have been studied by recording their field-cooled (FC) and zero-field-cooled (ZFC) magnetization curves in a DynaCool PPMS system under different applied magnetic fields. The biocompatibility of the uncovered Fe_3O_4 and gold coated Fe_3O_4 NPs have been evaluated on Madin Darby Canine Kidney (MDCK) cell line.

2. Experimental Procedure

2.1. Synthesis of Magnetic Nanoparticles

All the chemicals, ferric chloride hexahydrate ($FeCl_3{\cdot}6H_2O$), ferrous chloride tetrahydrate ($FeCl_2{\cdot}4H_2O$), oleic acid (OA), oleylamine (OAm), tetramethylammonium hydroxide pentahydrate (TMAH5, $C_4H_{13}NO{\cdot}5H_2O$), sodium borohydride ($NaBH_4$), and gold(III) chloride trihydrate ($HAuCl_4{\cdot}3H_2O$) of reagent grade were purchased from Sigma-Aldrich, Mexico, and utilized as received, without further purification.

Fe_3O_4 nanoparticles were obtained by solvothermal method. In a typical experimental procedure, 10 mL of 1 M $FeCl^{3+}$ aqueous solution was mixed with 5 mL of 1 M $FeCl^{2+}$ solution in a round bottom flask and heated to 70 °C under magnetic agitation. Keeping the mixture solution under magnetic agitation, about 9 mL of 3 M TMAH5 aqueous solution was added to the mixture slowly, to reach a pH of 11. Thereafter, about 1 mL of OA solution (50 mM) and 1 mL of OAm (50 mM) solution were added to the reaction mixture. The reaction continued at 70 °C for 20 min and then cooled down to room temperature naturally. Nanoparticles from the back colloidal solution were separated by a neodymium magnet and washed 3 times with ethanol.

After, $HAuCl_4$ (3 mL, 50 mM) was gradually reduced by $NaBH_4$ in 9 mL of the black solution of nanoparticles to form a thin Au shell on the Fe_3O_4 nanoparticle surface. The mixture was heated to 70 °C under vigorous stirring and cooled down to room temperature naturally. Again, the Fe_3O_4-Au nanoparticles were separated by a neodymium magnet and washed to eliminate the excess of reagents chemicals.

2.2. Characterization Methods

Fabricated magnetic nanoparticles were analyzed by X-ray diffraction (Rigaku Ultima IV), using CuKα (l = 1.5406 Å) radiation. Measurements were performed in parallel-beam geometry with 2θ scans from 15 to 80°. Fourier transform infrared spectroscopy (Bruker Vector 33) was used to study interactions between oleic acid (OA) and oleylamine (OAm) with the magnetic nanoparticles. The structural characterization of the as-prepared Fe_3O_4 and Fe_3O_4@Au NPs was carried out by electron microscopy. For electron microscopic observations, the samples were prepared by dispersing a drop of colloidal solution of the nanostructures over carbon coated copper grids. The samples were analyzed in a Jeol JEM-ARM200F scanning transmission electron microscope (STEM) equipped with a CEOS Cs-corrector as probe-corrector for STEM, operating at 200 keV. High-angle annular dark-field (HAADF)-STEM images were registered using a camera length of 80 mm and a collection angle of 50–180 mrad. HAADF-STEM image simulations have been performed using the QSTEM software package [29], which uses the multislice algorithm [30]. The parameters considered for the simulation were obtained from the experimental conditions of the microscope. A vibrating sample magnetometer (VSM) attached to a Physical Property Measurements System (PPMS, Quantum Design, Dyna-cool 9, USA) was used for all the magnetic measurements by placing the samples into tubular plastic sample holders.

2.3. Apoptosis Assay

Madin Darby Canine Kidney (MDCK) cells were cultured in 24-well plates. After subjecting the cells to the appropriate treatment (NaF and OTA), apoptotic/necrotic rate was determined by two flow cytometric methods. An Annexin V-FITC kit, which includes propidium iodide (PI) level was utilized for the fluorescence detection of Annexin V bound apoptotic cells and quantitative determination by flow cytometry, as described by N. Sali [31]. Briefly, any detached cell in the medium was carefully removed and spared for later analysis. Cells still attached to the culture plate surface were rinsed with phosphate-buffered saline (PBS) and trypsinized, then combined with the previously aspirated medium. Cell pellets after a short pulse centrifugation (3 s at 14,000 rpm) were re-suspended in 50 μL Annexin V binding buffer (10 mM HEPES, 140 mM NaCl, 2.5 mM $CaCl_2$, pH 7.4) and were incubated with 2.5 μL of FITC-Annexin V reagent (BD Pharmingen) and 5 μL of propidium iodide (PI) solution (50 μg/mL, Sigma-Aldrich) for 20 min at room temperature in the dark. Then 400 μL of binding buffer was added to the cell suspension and then the cells were analyzed by flow cytometry in a Beckton Dikinson flow cytometer using cell quest software. FITC-Annexin fluorescence versus PI fluorescence was analyzed.

3. Results and Discussion

There are many structures of iron oxide, such as: magnetite (Fe_3O_4), hematite (α-Fe_2O_3), maghemite (γ-Fe_2O_3), goethite (α-FeO(OH)), akaganeite (β-FeO(OH)) and lepidocrocite (γ-FeO(OH)) [12]. However, the

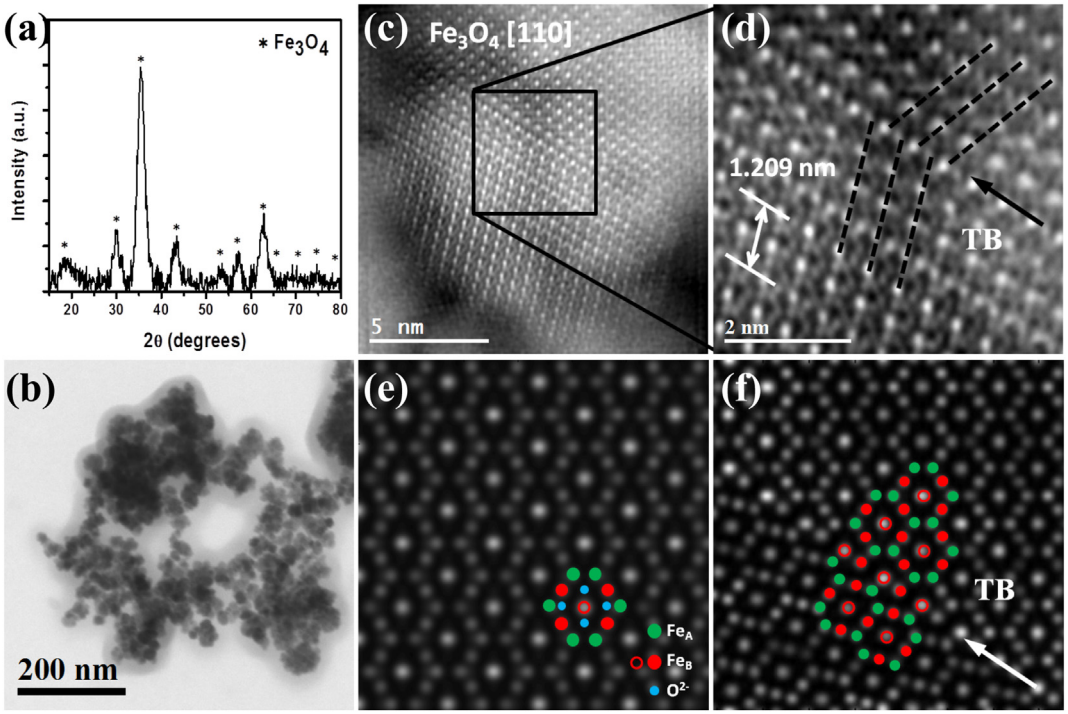

Fig. 1. (a) XRD pattern of the magnetic Fe_3O_4 nanoparticles, (b) BF-STEM image of the Fe_3O_4 nanoparticles, (c) and (d) High-resolution HAADF-STEM images of Fe_3O_4 nanoparticle. Simulated HAADF-STEM images of: (e) magnetite Fe_3O_4 structure and (f) twin boundary Fe_3O_4 structure. (For interpretation of the references to color in this figure, the reader is referred to the web version of this article.)

Fe_3O_4 and γ-Fe_2O_3 phases have similar crystal structures. In order to differentiate clearly, we performed both the structural and magnetic characterizations on the synthesized samples. Fig. 1a shows the experimental X-ray diffraction (XRD) pattern of the fabricated magnetite (Fe_3O_4). The XRD pattern of Fe_3O_4 clearly revealed diffraction peaks corresponding to its cubic phase and not other peaks were observed corresponding to other iron oxide phases like α-Fe_2O_3 and FeO(OH). The main diffraction peaks of the magnetite sample, located at 18.14, 30.14, 35.37, 43.12, 53.77, 57.06, 62.67, 73.90 and 74.87°, correspond to the (111), (220), (311), (400), (422), (511), (440), (533) and (622) planes of cubic Fe_3O_4 with spatial group Fd-3 m, respectively (JCPDS card no. 19-0629). Profex program [32] was used to calculate the crystallite size from the XRD pattern. The average crystallite size of the Fe_3O_4 nanoparticles was calculated using the half-maximum full width of the (311) plane and was estimated to be 22.5 nm. To characterize the morphology and fine structure of the Fe_3O_4 nanoparticles, scanning transmission electron microscopy (STEM) was performed. Fig. 1b shows a bright-field (BF)-STEM image of the nanoparticles. The STEM image of the sample exhibited some grade of aggregated morphology, which might be due to the use of oleic acid and oleylamine in excess during the synthesis process. Formation of organic cover over the particles can be observed clearly in the image. The particles showed irregular morphologies with diameter varying in the range of 20–50 nm. However, in spite of their aggregation, and the presence of organic cover, the nanoparticles maintained their superparamagnetic behaviour, as has been demonstrated later. The magnetite nanoparticles were sonicated in an ultrasonic bath for about 30 min, prior to the formation of Au covers over them, to ensure their dispersion through the dissociation of aggregates.

Fig. 1c shows an atomic resolution high-angle annular dark-field (HAADF)-STEM image of a Fe_3O_4 nanoparticle along the [110] zone axis. In this zone axis, the octahedral and tetrahedral iron (Fe) atoms of the Fe_3O_4 phase can be observed as separate atomic columns, which form hexagonal units with a central bright column. The HAADF-STEM image shows a twin boundary (TB) around the (111) plane (Fig. 1d). This indicates that the formation energy of twins defects on the (111) plane of the Fe_3O_4 phase is low [33]. From the image, the distance along [110] direction was estimated to be 1.209 nm, which is close to the value of the Fe_3O_4 bulk parameter $a_0 = 0.8396$ nm ($d_{110} = 0.8396 \times \sqrt{2} = 1.1873$ nm) [34]. All the spots in the figure correspond to Fe atomic column; the image contrast corresponding to Fe atoms has a strong brightness in comparison with the contrast corresponding to oxygen (O) atoms, which is unnoticed due to the large difference in atomic number of both elements.

Simulated electron microscopy images are useful to characterize the structure, and in some cases, to obtain the composition of a sample. For example, qualitative and quantitative analyses are now possible in simulated HAADF-STEM images [35]. Fig. 1e shows the simulated HAADF-STEM image of the Fe_3O_4 structure oriented along the [110] zone axis, obtained by QSTEM multislice image program, using 30 thermal diffuse scattering (TDS) runs and the experimental aberration values of the microscope. As can be observed, the experimental and simulated images are in good agreement. The presence of hexagonal units with a central column, observed in the experimentally obtained HAADF-STEM image, is consistent with the cubic structure of Fe_3O_4, with spatial group Fd-3 m. The high brightness of the columns is associated mainly with the octahedral (Fe_B) sites (the atomic positions are highlighted in the figure). This contrast is obtained by the atomic density of the Fe columns, given that the thickness of the sample is almost constant, particularly in this zone axis, where the central atomic column of Fe_B sites (open red circle) has the double of atoms that the atomic columns of the tetrahedral (Fe_A, solid green circle) sites and some Fe_B sites (solid red circle), which are situated around the central Fe_B sites. It is important to mention that when light and heavy elements coexist in the material, the contrast of the light elements is almost invisible in a HAADF-STEM image due to weak scattering of transmitted electrons by lighter elements. Such is the case for the O and Fe atoms in Fe_3O_4. The image contrast of O atoms is very weak, given that Fe has an atomic number (26), much higher than the atomic number (8) of O, making it difficult to determine the position of the O atoms in the

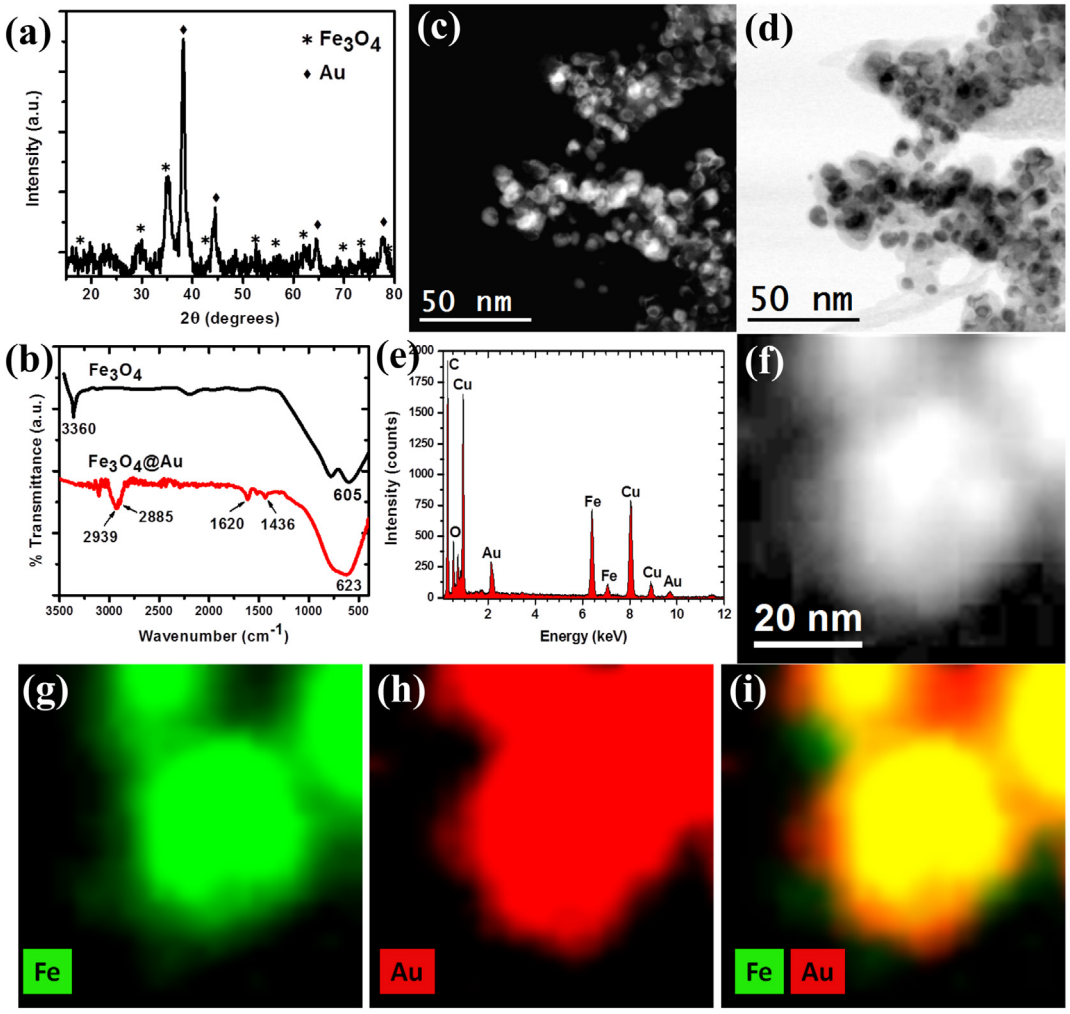

Fig. 2. (a) XRD pattern of the magnetic Fe_3O_4-Au nanoparticles, (b) FT-IR spectra of Fe_3O_4 and Fe_3O_4@Au, (c) HAADF-STEM and (d) BF-STEM images of the magnetic Fe_3O_4@Au nanoparticles, (e) EDS spectrum of the nanoparticles, (f) HAADF-STEM image of Fe_3O_4@Au nanoparticles, EDS mapping revealed the elemental distributions: (g) Fe (green), (h) Au (red), and their (i) superposition. (For interpretation of the references to color in this figure legend, the reader is referred to the web version of this article.)

HAADF-STEM image of Fe_3O_4.

Simulation of HAADF-STEM images was also performed to determine the atomic characteristics of the twin boundary. Fig. 1f shows the simulated HAADF-STEM image of the twin defect around the (111) plane of the Fe_3O_4 structure. The Fe atomic positions around the twin boundary are highlighted, with Fe_A sites in solid green circles and Fe_B sites in open and solid red circles. As can be observed, the twin boundary appears in the octahedral Fe_B sites. It is interesting to notice that the brightness contrast of the twin boundary is similar to the contrast in experimental image (Fig. 1d). The images show atomic columns with high brightness contrast, which is an associate with the Fe_B sites with high atomic density (open red circle).

Fig. 2a shows the experimental XRD pattern of the fabricated gold (Au) coated magnetite (Fe_3O_4@Au) nanoparticles. In the diffraction pattern, the peaks corresponding of Fe_3O_4 along with the peaks correspond to Au in cubic phase appeared. The characteristic Au peaks appeared around 38, 44.2, 64.7 and 77.5° correspond to the (111), (200), (220) and (311) planes of Au in cubic phase, respectively (JCPDS card no. 04-0784). The XRD pattern revealing diffraction peaks of both Au and Fe_3O_4 structures validates a successful formation of Fe_3O_4-Au composite structure. In addition, the intensities of Fe_3O_4 structure decreased compared with those of the Fe_3O_4, while the intensities of Au increased due to the heavy atom effect of Au [19]. The amount of Fe_3O_4 and Au phases calculated from the XRD were 79.16 wt% and 20.84 wt %, respectively.

The surface chemistry of the Fe_3O_4 and Fe_3O_4-Au nanoparticles was studied using Fourier-transform infrared spectroscopy (FT-IR). In this case to confirm the presence of OA, OAm and Au on the Fe_3O_4 nanoparticles surface, uncoated Fe_3O_4 nanoparticles without OA, OAm and Au were used. Fig. 2b shows the FT-IR spectra of uncoated Fe_3O_4 and Fe_3O_4@Au nanoparticles in the range of 3500–400 cm^{-1}. FT-IR spectrum of uncoated Fe_3O_4 nanoparticles shows a peak at 605 cm^{-1} that is attributed to the vibration of the Fe—O functional group, and the band at 3360 cm^{-1} is assigned to OH stretching vibration which is due to adsorbed water on the surface of the iron oxide nanoparticles. FT-IR spectrum of Fe_3O_4@Au nanoparticles shows a band at 623 cm^{-1} that is assigned to the Fe—O stretching vibrations of Fe_3O_4, and its intensity in comparison with uncoated Fe_3O_4 is decreased due to gold coating [36]. The strong CH_2 peaks at 2939 (ν_{as} C—H), 2885 (ν_s C—H), 1436 (δ_s C—H) and 1620 cm^{-1} (ν C=C) are indicative of both molecules of OA and OAm that cover the iron oxide nanoparticles [37].

Fig. 2c and d present the typical HAADF-STEM and BF-STEM images of the magnetic Fe_3O_4@Au nanoparticles, respectively. The difference in contrast between the magnetite core and metallic shell is clear in both the images. However, this can observe clearly from Fig. 2c, where the contrast of the image is associated with the atomic number. In this case, the brightness is associated to the Au atoms. Therefore, from the images it is confirmed that the majority of the Fe_3O_4@Au nanoparticles

obtained through our synthesis process have core-shell structure. In addition, Fig. 2d shows a small layer around all the nanoparticles, which is the organic layer, appearing from oleic acid and oleylamine that were used as reducing agent and stabilizer, respectively [38].

The elemental distribution in the Fe_3O_4 nanoparticles covered with Au was analyzed by STEM-energy dispersive spectroscopy (STEM-EDS). Fig. 2e shows a typical EDS spectrum of the Fe_3O_4@Au nanoparticles. The EDS spectrum demonstrates that the Fe_3O_4@Au nanoparticles consist of C, O, Fe and Au elements (Cu signal appeared from the copper grid). The detected carbon signal was assumed to be originated from the sample (oleic acid and oleylamine) and the support films of the grid. The quantification of Fe, O and Au elements was 57.87, 24.01 and 18.12 wt%, respectively. These values are close to those determined by the XRD analysis. EDS was employed to obtain the distribution of Fe and Au elements in the sample. Fig. 2f corresponds to the HAADF-STEM image of a Fe_3O_4@Au nanoparticle. This image shows some differences in the contrast which are related with the elements. For example, the presence of Au atoms which have a higher Z than the Fe_3O_4 particles, are displayed with brighter regions. Fig. 2g and h show the STEM-EDS mapping of the elemental, revealing the distribution of iron (green) and gold (red), respectively. The superposed HAADF-STEM image presented in Fig. 2i confirms the formation of Fe_3O_4@Au core-shell structure.

HAADF-STEM is the only technique where the intensity contrast of the images exhibits strong dependence with the atomic number (Z). Fig. 3a and b show images of Fe_3O_4@Au core-shell structure. In these images, the contrast of the Fe_3O_4 core is very weak in comparison with the Au shell. This is due to the large difference in atomic number; the columns of light elements in presence of heavy elements are difficult to visualize, because of the intensity of the image in HAADF-STEM is dominated by the thermal diffuse scattering (TDS), which favours the visualization of heavy elements [39]. Fig. 3c shows a high-resolution HAADF-STEM image from a region of the Fe_3O_4@Au core-shell nanoparticle. The presence of both structures Fe_3O_4 and the Au shell is clear in this image. The lattice fringes correspond to the inter-planar (d) spacing of Au estimated to be about 0.204 nm, which corresponds to the (200) planes of the Au in cubic phase (JCPDS card no. 04-0784) and the fringe spacings in the core is about 0.263 nm, corresponds to Fe_3O_4 in cubic phase (JCPDS card no. 19-0629). It is interesting to observe the interface between the core and the shell; the crystalline planes are interconnected and no crystalline defects such as planar dislocation are observable. The images of materials with an interface between light and heavy elements are difficult to estimate. Recently, annular bright-field (ABF)-STEM has been successfully used to visualize columns of light elements [40]. However, in this image, the interface between the Fe_3O_4 core and Au shell can be clearly visualized. It is important to mention that even after more than six months of fabrication of the Fe_3O_4@Au nanoparticles (images were recorded after 6 months), their structural and magnetic properties were maintained. On the other hand, the structure of Fe_3O_4 nanoparticles synthesized without Au shell changed within a month of their fabrication, due to oxidation process. The Fe_3O_4 phase was transformed to γ-Fe_2O_3 and α-Fe_2O_3 phases. Thermodynamically, the Fe_2O_3 phase is more stable than the Fe_3O_4 phase; the reaction of oxidation of the Fe_3O_4 to Fe_2O_3 is exothermic and may take place at room temperature [41]. Therefore, the Fe_3O_4@Au core-shell nanoparticles are structurally and magnetically very stable for prolonged period, thereby enhancing their chemical stability and biocompatibility, providing a solid platform to be used as a contrast agent or for the application in therapeutic treatments [42]. HAADF-STEM along with image simulation are important tools for the determination of structure, composition, morphology and atomic positions of nanomaterials [43,44]. Fig. 3d shows a simulated HAADF-STEM image from a Fe_3O_4@Au model. The parameters used in the simulated image were

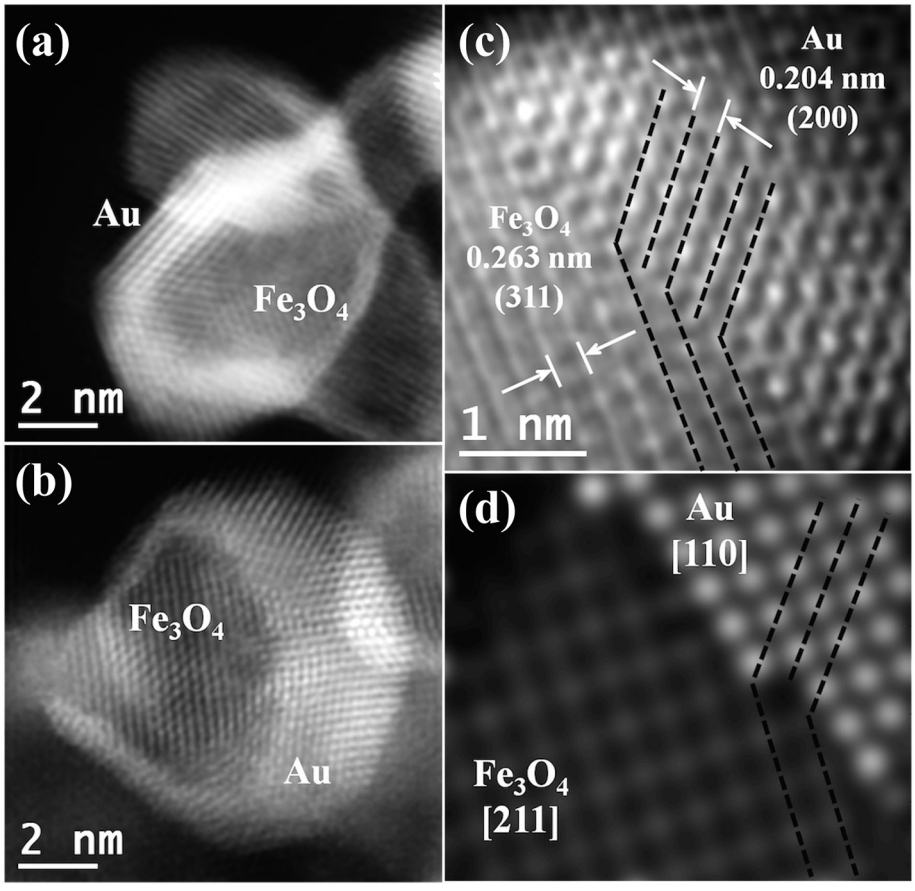

Fig. 3. (a), (b) and (c) High-resolution HAADF-STEM images of Fe_3O_4@Au core-shell nanoparticles and (d) Simulated HAADF-STEM image of Fe_3O_4@Au model.

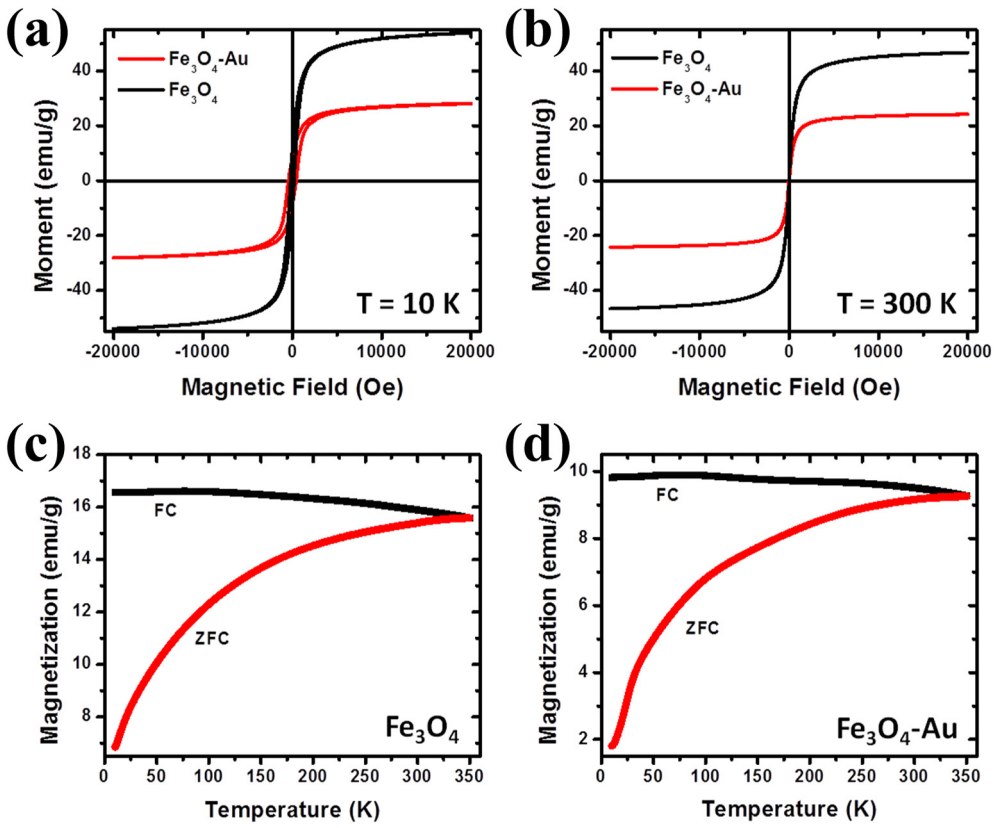

Fig. 4. Hysteresis loops of Fe_3O_4 and Fe_3O_4@Au nanoparticles at: (a) 10 and (b) 300 K, ZFC and FC magnetization curves for (c) Fe_3O_4 and (d) Fe_3O_4@Au nanoparticles.

obtained from the conditions of the electron microscope. The simulated image matches perfectly with the experimental image, and also shows the contrast difference between the Fe_3O_4 and Au phases; they are oriented in [211] and [110] zone axis, respectively. To obtain the similar contrast between the experimental and simulated images, the model was made by overlaying two Fe_3O_4 structures. The Au shell was made stacking few layers around the Fe_3O_4 core.

The magnetic measurements on the fabricated nanostructures were performed at different temperatures ranging from 300 to 10 K. The M-H curves obtained for Fe_3O_4 and Fe_3O_4@Au nanoparticles are presented in Figs. 4a and b, respectively. As can be seen, while the hysteresis of both the samples revealed superparamagnetic behaviour at 300 K (Fig. 4b), at 10 K both the samples revealed mild remanent magnetization (*Mr*) and coercivity (*Hc*) (Fig. 4a). While the *Mr* and *Hc* values for the Fe_3O_4 nanoparticles were estimated to be ≈54 emu/g and 20 Oe for Fe_3O_4, respectively, those values estimated for Fe_3O_4@Au NPs were ≈28 emu/g and 420 Oe, respectively. As expected, the saturation magnetization of the magnetite nanoparticles decreased due to Au coating over them [45,46].

Fig. 4c and d show the field cooling (FC) and zero field cooling (ZFC) curves of the uncovered Fe_3O_4 and Au-coated Fe_3O_4 nanoparticles, respectively, in 10 to 350 K temperature range. While the FC curve of the Au-coated Fe_3O_4 NPs revealed maximum magnetization a bit lower than the maximum magnetization of the uncovered Fe_3O_4 NPs as expected, there was no indication of any change in the blocking temperature of the magnetite NPs due to gold coating. While a clear and well-defined maximum in the ZFC curve for either of the samples could not be detected in the measured temperature range, a blocking temperature of ≈325 K can assumed for both the samples from the shape of their ZFC curves.

The obtained results indicate that the formation of Au shell over Fe_3O_4 nanoparticles does not change their superparamagnetic behaviour. The decrease of *Mr* value of the Fe_3O_4 NPs due to Au coating can be attributed to the non-magnetic nature of Au, spin canting at the surface or even to a surface spin-glass transition [19,47]. Specifically, in this case, it can be explained in terms of a chemical bonding of the non-magnetic material (Au) and the organic molecules (oleic acid and oleylamine) added to the Fe_3O_4 nanostructures, which decrease the magnetization of the surface layers.

As the utilization of Fe_3O_4 and Fe_3O_4@Au NPs in biomedical applications depends strongly on their compatibility with biological cells, i.e. they should not be toxic to the target cells [48], we performed cytotoxicity tests of the fabricated nanostructures over Madin Darby Canine Kidney (MDCK) cells through apoptosis assays (early apoptosis and late apoptosis) by flow cytometry, based on propidium iodide/Annexin V-FITC staining patterns. Fig. 5 shows the representative dot plots for the flow cytometric analysis comparing untreated cells (control) and treated cells after 48 h of cultivation. After the cultivation period, the apoptosis rate for the control group (Fig. 5a) was 4.93%. Annexin V+/PI− (lower right quadrant) areas stand for early apoptotic cells, and Annexin V+/PI+ (upper right quadrant) areas stand for late apoptotic or necrotic cells. Apoptosis rate include early apoptotic cells and late apoptotic or necrotic cells. However, when the cells were treated with Fe_3O_4 nanoparticles, an increase in the percentages of early apoptosis and late apoptosis was observed. As shown in Fig. 5b, treatments with 0.5, 1 and 2 μL of Fe_3O_4 nanoparticles caused an increase in the percentage of apoptosis rate; from 32.18% to 40.33% (Fig. 5c). On the other hand, when the cells were treated with Fe_3O_4@Au nanoparticles, a significant decrease in the percentages in early apoptosis and late apoptosis with respect to untreated cells was observed. The results show interesting physical properties that correlate with the forms and structures found in our magnetic NPs and we propose to use it for various biomedical applications.

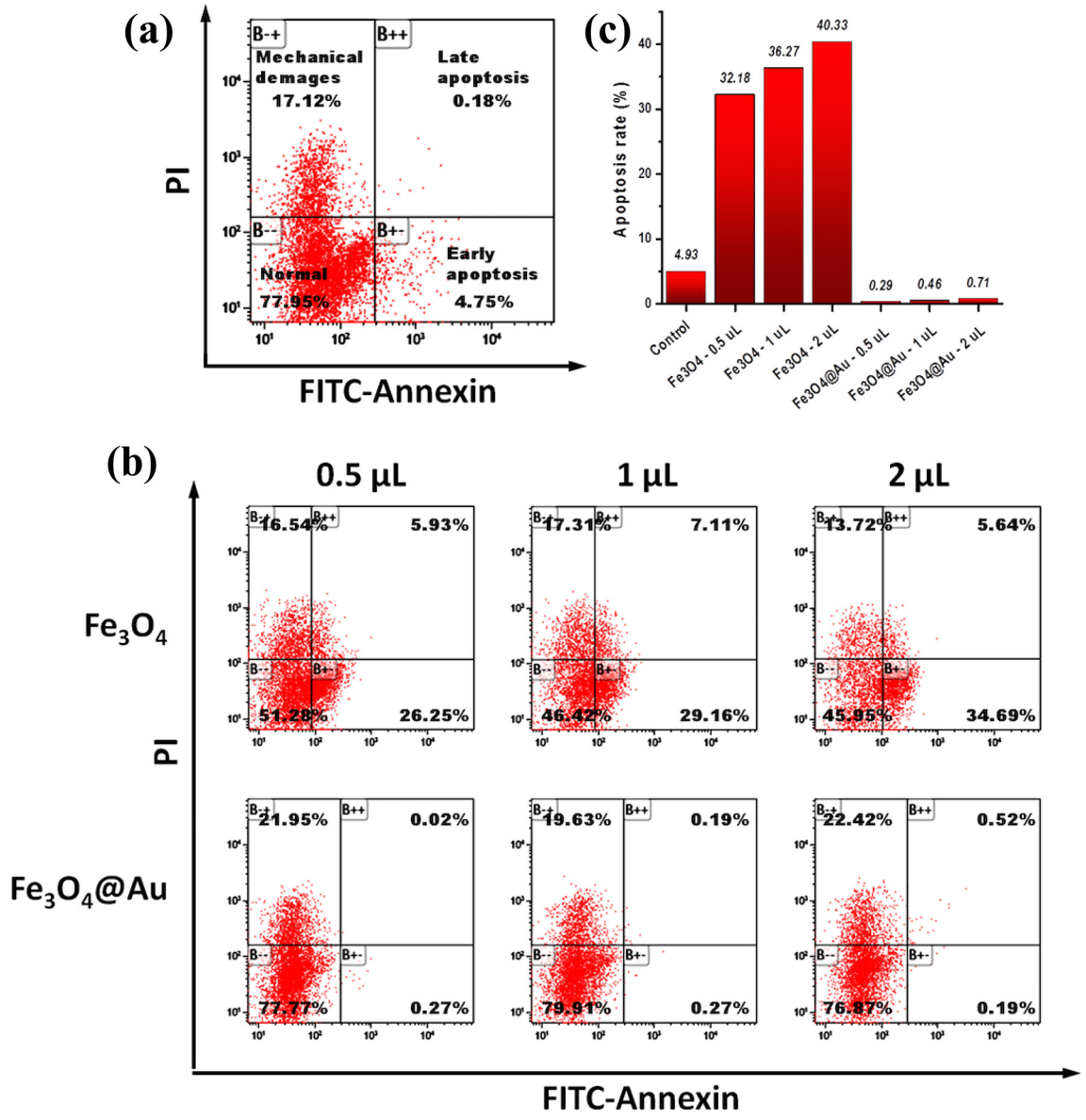

Fig. 5. Annexin V-FITC apoptosis assay for determining the effect of Fe_3O_4 and Fe_3O_4@Au nanoparticles on apoptosis/necrosis in MDCK cells using flow cytometry, (a) control, (b) 0.5, 1 and 2 µL of nanoparticles solution, and (c) apoptosis rate.

4. Conclusions

Core-shell Fe_3O_4@Au nanoparticles of 20–50 nm sizes were synthesized by a novel, economical and efficient one-pot solvothermal method. The cubic structure of the nanoparticles was determined using XRD and aberration corrected (Cs) STEM techniques. HAADF images of the nanoparticles acquired in STEM mode revealed the principal contribution (high brightness) of octahedral and tetrahedral Fe sites in their image contrast. STEM-EDS confirms the Fe_3O_4 core and Au shell structure of the magnetic nanoparticles. Cytotoxicity tests of Fe_3O_4 and Fe_3O_4@Au nanoparticles probed on MDCK cells revealed a significant toxicity with an apoptotic response for the uncovered Fe_3O_4 particles, the apoptosis rate increase from 4.93% for the control group to 40.33% for uncovered Fe_3O_4 particles. On the other hand, Fe_3O_4@Au nanoparticles showed low apoptotic response, with an apoptosis rate of 0.71%, demonstrating their lower toxicity. Fabricated Fe_3O_4@Au nanoparticles of superparamagnetic nature, with high saturation magnetization and good biocompatibility, offer a great promise for their biomedical applications such as in magnetic resonance imaging (MRI), photo-thermal therapy, magnetic hyperthermia and anticancer therapy.

Acknowledgments

The authors thank to Genoveva Hernández for the support in the spectroscopy characterization, S. Kumar and A.L. Rodríguez-Morales for the support in the magnetic measurements, and Víctor Rosales-García for the support in the apoptosis assay. Also, the authors would like to acknowledge to the Laboratorio Nacional de Caracterización de Materiales (LaNCaM) at the CFATA-UNAM, to the Laboratorio Avanzado de Nanoscopía Electrónica (LANE) and Laboratorio Nacional de Servicios Experimentales (LaNSE) at the CINVESTAV-Zacatenco. The work was partially supported by CONACyT, Mexico (Grant # INFR-2014-02-23053).

References

[1] J. Shan, L. Wang, H. Yu, J. Ji, W. Amer, Y. Chen, G. Jing, H. Khalid, M. Akram, N. Abbasi, Recent progress in Fe_3O_4 based magnetic nanoparticles: from synthesis to application, Mater. Sci. Technol. 32 (2016) 602–614.
[2] M.R. Ghazanfari, M. Kashefi, S.F. Shams, M.R. Jaafari, Perspective of Fe_3O_4 nanoparticles role in biomedical applications, Biochem. Res. Int. 2016 (2016).
[3] L. Landgraf, I. Müller, P. Ernst, M. Schäfer, C. Rosman, I. Schick, O. Köhler,

H. Oehring, V.V. Breus, T. Basché, Comparative evaluation of the impact on endothelial cells induced by different nanoparticle structures and functionalization, Beilstein J. Nanotechnol. 6 (2015) 300.
[4] E.R. Encina, E.A. Coronado, Size optimization of Iron oxide@ noble metal core–shell nanohybrids for photothermal applications, J. Phys. Chem. C 120 (2016) 5630–5639.
[5] L. Zhou, J. Yuan, Y. Wei, Core–shell structural iron oxide hybrid nanoparticles: from controlled synthesis to biomedical applications, J. Mater. Chem. 21 (2011) 2823–2840.
[6] S.V. Salihov, Y.A. Ivanenkov, S.P. Krechetov, M.S. Veselov, N.V. Sviridenkova, A.G. Savchenko, N.L. Klyachko, Y.I. Golovin, N.V. Chufarova, E.K. Beloglazkina, Recent advances in the synthesis of Fe_3O_4@Au core/shell nanoparticles, J. Magn. Magn. Mater. 394 (2015) 173–178.
[7] O.K. Arriortua, E. Garaio, B.H. de la Parte, M. Insausti, L. Lezama, F. Plazaola, J.A. García, J.M. Aizpurua, M. Sagartzazu, M. Irazola, Antitumor magnetic hyperthermia induced by RGD-functionalized Fe_3O_4 nanoparticles, in an experimental model of colorectal liver metastases, Beilstein J. Nanotechnol. 7 (2016) 1532.
[8] J. Mazo-Zuluaga, J. Restrepo, J. Mejía-López, Surface anisotropy of a Fe_3O_4 nanoparticle: a simulation approach, Phys. B Condens. Matter 398 (2007) 187–190.
[9] G. Mirabello, J.J. Lenders, N.A. Sommerdijk, Bioinspired synthesis of magnetite nanoparticles, Chem. Soc. Rev. 45 (2016) 5085–5106.
[10] S. Lee, J. Jeong, S. Shin, J.C. Kim, J.D. Kim, Synthesis and characterization of superparamagnetic maghemite nanoparticles prepared by coprecipitation technique, J. Magn. Magn. Mater. 282 (2004) 147–150.
[11] H. Shirazi, M. Daneshpour, S. Kashanian, K. Omidfar, Synthesis, characterization and in vitro biocompatibility study of Au/TMC/Fe_3O_4 nanocomposites as a promising, nontoxic system for biomedical applications, Beilstein J. Nanotechnol. 6 (2015) 1677.
[12] S. Jain, D. Hirst, J. O'sullivan, Gold nanoparticles as novel agents for cancer therapy, Br. J. Radiol. 85 (2012) 101–113.
[13] H.-C. Huang, S. Barua, G. Sharma, S.K. Dey, K. Rege, Inorganic nanoparticles for cancer imaging and therapy, J. Control. Release 155 (2011) 344–357.
[14] C.J. Murphy, A.M. Gole, J.W. Stone, P.N. Sisco, A.M. Alkilany, E.C. Goldsmith, S.C. Baxter, Gold nanoparticles in biology: beyond toxicity to cellular imaging, Acc. Chem. Res. 41 (2008) 1721–1730.
[15] R. Ankri, V. Peretz, M. Motiei, R. Popovtzer, D. Fixler, A new method for cancer detection based on diffusion reflection measurements of targeted gold nanorods, Int. J. Nanomedicine 7 (2012) 449.
[16] X. Huang, P.K. Jain, I.H. El-Sayed, M.A. El-Sayed, Plasmonic photothermal therapy (PPTT) using gold nanoparticles, Lasers Med. Sci. 23 (2008) 217.
[17] H. Guo, A.S. Barnard, Naturally occurring iron oxide nanoparticles: morphology, surface chemistry and environmental stability, J. Mater. Chem. A 1 (2013) 27–42.
[18] L. Li, M. Nurunnabi, M. Nafiujjaman, Y.Y. Jeong, Y.-k. Lee, K.M. Huh, A photosensitizer-conjugated magnetic iron oxide/gold hybrid nanoparticle as an activatable platform for photodynamic cancer therapy, J. Mater. Chem. B 2 (2014) 2929–2937.
[19] Z. Xu, Y. Hou, S. Sun, Magnetic core/shell Fe_3O_4/Au and Fe_3O_4/Au/Ag nanoparticles with tunable plasmonic properties, J. Am. Chem. Soc. 129 (2007) 8698–8699.
[20] Y. Lee, M.A. Garcia, N.A. Frey Huls, S. Sun, Synthetic tuning of the catalytic properties of Au-Fe_3O_4 nanoparticles, Angew. Chem. 122 (2010) 1293–1296.
[21] P. Alonso-Cristobal, M. Laurenti, E. Lopez-Cabarcos, J. Rubio-Retama, Efficient synthesis of core@ shell Fe_3O_4@Au nanoparticles, Mater. Res. Express 2 (2015) 075002.
[22] F. Li, Z. Yu, L. Zhao, T. Xue, Synthesis and application of homogeneous Fe_3O_4 core/Au shell nanoparticles with strong SERS effect, RSC Adv. 6 (2016) 10352–10357.
[23] R. Jin, D. Song, H. Xiong, L. Ai, P. Ma, Y. Sun, Magnetic core/shell Fe_3O_4/Au nanoparticles for studies of quinolones binding to protein by fluorescence spectroscopy, Luminescence 31 (2016) 499–506.
[24] Y. Hu, R. Wang, S. Wang, L. Ding, J. Li, Y. Luo, X. Wang, M. Shen, X. Shi, Multifunctional Fe_3O_4@Au core/shell nanostars: a unique platform for multimode imaging and photothermal therapy of tumors, Sci. Rep. 6 (2016) 28325.
[25] F. Mohammad, G. Balaji, A. Weber, R.M. Uppu, C.S. Kumar, Influence of gold nanoshell on hyperthermia of superparamagnetic iron oxide nanoparticles, J. Phys. Chem. C 114 (2010) 19194–19201.
[26] A.K. Gupta, M. Gupta, Synthesis and surface engineering of iron oxide nanoparticles for biomedical applications, Biomaterials 26 (2005) 3995–4021.
[27] Y. Li, J. Liu, Y. Zhong, J. Zhang, Z. Wang, L. Wang, Y. An, M. Lin, Z. Gao, D. Zhang, Biocompatibility of Fe_3O_4@ Au composite magnetic nanoparticles in vitro and in vivo, Int. J. Nanomedicine 6 (2011) 2805.
[28] X. Chao, F. Shi, Y.-Y. Zhao, K. Li, M.-L. Peng, C. Chen, Y.-L. Cui, Cytotoxicity of Fe_3O_4/Au composite nanoparticles loaded with doxorubicin combined with magnetic field, Pharmazie 65 (2010) 500–504.
[29] C.T. Koch, Determination of Core Structure Periodicity and Point Defect Density along Dislocations, (2002).
[30] J.M. Cowley, A.F. Moodie, The scattering of electrons by atoms and crystals. I. A new theoretical approach, Acta Crystallogr. 10 (1957) 609–619.
[31] N. Sali, S. Nagy, M. Poór, T. Kőszegi, Multiparametric luminescent cell viability assay in toxicology models: a critical evaluation, J. Pharmacol. Toxicol. Methods 79 (2016) 45–54.
[32] N. Doebelin, R. Kleeberg, Profex: a graphical user interface for the Rietveld refinement program BGMN, J. Appl. Crystallogr. 48 (2015) 1573–1580.
[33] D. Gilks, L. Lari, K. Matsuzaki, R. Evans, K. McKenna, T. Susaki, V. Lazarov, A STEM study of twin defects in Fe_3O_4(111)/YZO(111), J. Phys. Conf. Ser. (2014) 012036 IOP Publishing.
[34] H. Xiang, F.-Y. Shi, C. Zhang, M. Rzchowski, P. Voyles, Y. Chang, Synthesis of Fe_3O_4 thin films by selective oxidation with controlled oxygen chemical potential, Scr. Mater. 65 (2011) 739–742.
[35] S. Van Aert, J. Verbeeck, R. Erni, S. Bals, M. Luysberg, D. Van Dyck, G. Van Tendeloo, Quantitative atomic resolution mapping using high-angle annular dark field scanning transmission electron microscopy, Ultramicroscopy 109 (2009) 1236–1244.
[36] S. Karamipour, M. Sadjadi, N. Farhadyar, Fabrication and spectroscopic studies of folic acid-conjugated Fe_3O_4@Au core–shell for targeted drug delivery application, Spectrochim. Acta A Mol. Biomol. Spectrosc. 148 (2015) 146–155.
[37] K. Simeonidis, S. Mourdikoudis, I. Tsiaoussis, M. Angelakeris, C. Dendrinou-Samara, O. Kalogirou, Structural and magnetic features of heterogeneously nucleated Fe-oxide nanoparticles, J. Magn. Magn. Mater. 320 (2008) 1631–1638.
[38] Z. Xu, C. Shen, Y. Hou, H. Gao, S. Sun, Oleylamine as both reducing agent and stabilizer in a facile synthesis of magnetite nanoparticles, Chem. Mater. 21 (2009) 1778–1780.
[39] A. Lotnyk, D. Poppitz, J.W. Gerlach, B. Rauschenbach, Direct imaging of light elements by annular dark-field aberration-corrected scanning transmission electron microscopy, Appl. Phys. Lett. 104 (2014) 071908.
[40] D. Kan, R. Aso, H. Kurata, Y. Shimakawa, Research update: Interface-engineered oxygen octahedral tilts in perovskite oxide heterostructures, APL Mater. 3 (2015) 062302.
[41] E.R. Monazam, R.W. Breault, R. Siriwardane, Kinetics of magnetite (Fe_3O_4) oxidation to hematite (Fe_2O_3) in air for chemical looping combustion, Ind. Eng. Chem. Res. 53 (2014) 13320–13328.
[42] X. Shen, Z. Ge, Y. Pang, Conjugating folate on superparamagnetic Fe_3O_4@Au nanoparticles using click chemistry, J. Solid State Chem. 222 (2015) 37–43.
[43] R. Aveyard, R. Ferrando, R.L. Johnston, J. Yuan, Modeling nanoscale inhomogeneities for quantitative HAADF STEM imaging, Phys. Rev. Lett. 113 (2014) 075501.
[44] R. Esparza, O. Téllez-Vázquez, G. Rodríguez-Ortiz, A. Ángeles-Pascual, S. Velumani, R. Pérez, Atomic structure characterization of Au–Pd bimetallic nanoparticles by aberration-corrected scanning transmission electron microscopy, J. Phys. Chem. C 118 (2014) 22383–22388.
[45] M. Anbarasu, M. Anandan, E. Chinnasamy, V. Gopinath, K. Balamurugan, Synthesis and characterization of polyethylene glycol (PEG) coated Fe_3O_4 nanoparticles by chemical co-precipitation method for biomedical applications, Spectrochim. Acta A Mol. Biomol. Spectrosc. 135 (2015) 536–539.
[46] A.H. Lu, E.e.L. Salabas, F. Schüth, Magnetic nanoparticles: synthesis, protection, functionalization, and application, Angew. Chem. Int. Ed. 46 (2007) 1222–1244.
[47] P. An, F. Zuo, X. Li, Y. Wu, J. Zhang, Z. Zheng, X. Ding, Y. Peng, A bio-inspired polydopamine approach to preparation of gold-coated Fe_3O_4 core–shell nanoparticles: synthesis, characterization and mechanism, Nano 8 (2013) 1350061.
[48] H. Markides, M. Rotherham, A. El Haj, Biocompatibility and toxicity of magnetic nanoparticles in regenerative medicine, J. Nanomater. 2012 (2012) 13.